

A robust and interpretable deep learning framework for multi-modal registration via keypoints

Alan Q. Wang^{a,b,*}, Evan M. Yu^c, Adrian V. Dalca^{d,e}, Mert R. Sabuncu^{a,b}

^a*School of Electrical and Computer Engineering, Cornell University and Cornell Tech, New York, NY 10044, USA*

^b*Department of Radiology, Weill Cornell Medical School, New York, NY 10065, USA*

^c*Iterative Scopes, Cambridge, MA 02139, USA*

^d*Computer Science and Artificial Intelligence Lab at the Massachusetts Institute of Technology, Cambridge, MA 02139, USA*

^e*A.A. Martinos Center for Biomedical Imaging at the Massachusetts General Hospital, Charlestown, MA 02129, USA*

Abstract

We present KeyMorph, a deep learning-based image registration framework that relies on automatically detecting corresponding keypoints. State-of-the-art deep learning methods for registration often are not robust to large misalignments, are not interpretable, and do not incorporate the symmetries of the problem. In addition, most models produce only a single prediction at test-time. Our core insight which addresses these shortcomings is that corresponding keypoints between images can be used to obtain the optimal transformation via a differentiable closed-form expression. We use this observation to drive the end-to-end learning of keypoints tailored for the registration task, and without knowledge of ground-truth keypoints. This framework not only leads to substantially more robust registration but also yields better interpretability, since the keypoints reveal which parts of the image are driving the final alignment. Moreover, KeyMorph can be designed to be equivariant under image translations and/or symmetric with respect to the input image ordering. Finally, we show how multiple deformation fields can be computed efficiently and in closed-form at test time corresponding to different transformation variants. We demonstrate the proposed framework in solving 3D affine and spline-based registration of multi-modal brain MRI scans. In particular, we show registration accuracy that surpasses current state-of-the-art methods, especially in the context of large displacements. Our code is available at <https://github.com/evanmy/keymorph>.

Keywords: Image registration, Multi-modal, Keypoint detection

1. Introduction

Registration is a fundamental problem in biomedical imaging tasks. Multiple images, often reflecting a variety of contrasts, are commonly acquired in many applications (Uludağ and Roebroek, 2014). Classical (i.e. non-learning-based) registration methods involve an iterative optimization of a similarity metric over a space of transformations (Oliveira and Tavares, 2014; Sotiras et al.,

2013). An optional regularization term scaled by a hyper-parameter encourages smoothness of the transformation. Deep learning-based strategies leverage large datasets of images to solve registration and are able to perform fast inference via efficient feed-forward passes. These strategies use convolutional neural network (CNN) architectures that either output transformation parameters (e.g. affine or spline) (Lee et al., 2019b; de Vos et al., 2019) or a dense deformation field (Balakrishnan et al., 2019) which aligns an image pair.

However, we pinpoint several shortcomings of prior CNN-based methods:

*Corresponding author:

Email address: aw847@cornell.edu (Alan Q. Wang)

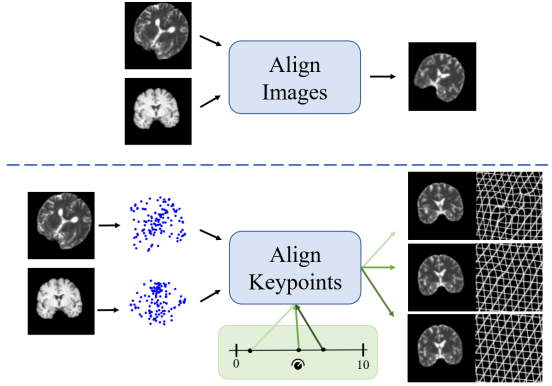


Figure 1: (Top) Existing registrations tools take as input a single moving and fixed image pair and output a single prediction by aligning images. These “black-box” models are often not robust to large initial misalignments and are hard to interpret. (Bottom) KeyMorph detects corresponding keypoints from input pairs and aligns the keypoints in an interpretable fashion. A knob allows for controllable user selection of many optimal registrations at test time corresponding to different degrees of nonlinearity.

- They often fail when the given image pair has a large misalignment (see Fig. 1). This is likely due to CNNs being unable to effectively learn long-range dependencies and correspondences. Existing systems typically require that image pairs are roughly aligned (Balakrishnan et al., 2019; Dalca et al., 2019; de Vos et al., 2019; Qin et al., 2019), or at least are in the same orientation (Mocanu et al., 2021).
- They lack interpretability, as they are essentially “black-box models” that output either transformation parameters or a deformation field and provide little insight into what drives the alignment.
- They generally do not exploit the symmetries and equivariances present in the problem. For example, if one of the images is translated by a fixed amount, this has a pre-determined effect on the optimal registration solution, and this property is not built into any of the architectures used today for image registration. Explicitly leveraging this inductive bias can improve performance and robustness.

Contribution. In this work, we present KeyMorph, an end-to-end deep learning-based framework that seeks to

address these aforementioned issues. The main insight is that *corresponding keypoints* can be used to derive the optimal transformation in closed-form, where the keypoints themselves are learned by a neural network. These keypoints are optimized specifically for the registration task, and we do not assume knowledge of ground-truth keypoints. Choosing a transformation whose optimal parameters can be solved in a differentiable manner given the learned keypoints enables end-to-end training of the registration pipeline. In a sentence, rather than treating matched keypoint detection as a supervised learning problem requiring human-annotated keypoints, we propose to use an end-to-end unsupervised strategy tailored toward registration.

This keypoint-based formulation is robust against misalignments as the closed-form solution is not sensitive to the initial position of the keypoints. Additionally, the model is interpretable since the keypoints that drive the alignment can be visualized. Furthermore, we also show how to incorporate symmetries into the model design. Finally, for a given transformation which accepts user-specified hyperparameters, a dense set of registrations can be computed at test-time directly from the learned keypoints, requiring no modulation of the neural network architecture. For example, the architecture we describe in this paper is translation-equivariant and leverages a recently-proposed center-of-mass layer (Ma et al., 2020; Sofka et al., 2017). We demonstrate this framework in the context of affine and spline-based registration of 3D multi-modal brain MR scans.

This work is an extension of our conference publication (Yu et al., 2022), which presented KeyMorph as a robust, unsupervised, affine registration method that aligns learned keypoints. In this work, we extend our previous submission to parametric, spline-based non-linear transformations with user-specified hyperparameters, and explore the controllability that this affords. Additionally, we provide a comprehensive treatment of both supervised and unsupervised variants, introduce new training strategies for unsupervised variants, and empirically demonstrate improved results.

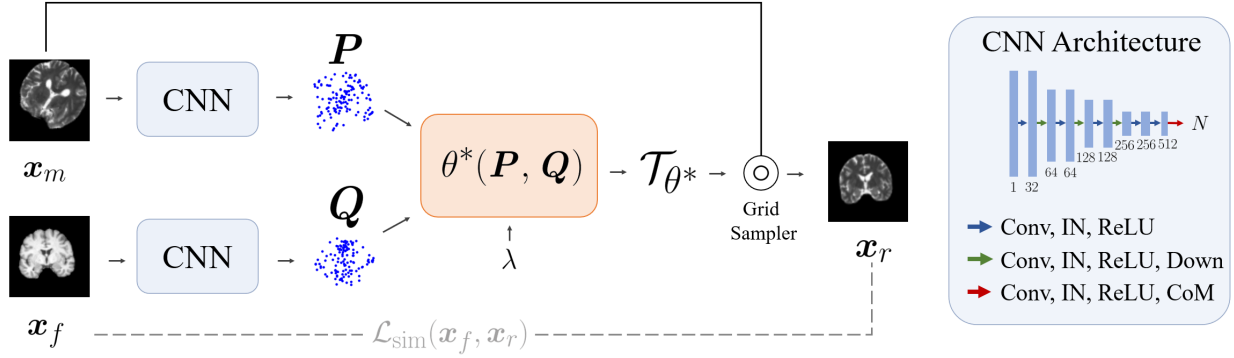


Figure 2: Proposed framework. Fixed and moving 3D images are passed through the same keypoint detection network composed of convolutional layers, instance normalization (IN), downsampling (Down), and a final center-of-mass (CoM) layer that predicts N keypoints useful for registration. The transformation parameters are then computed as a function of the keypoints, which are in turn used to resample the moving image.

2. Related Work

Classical Methods. Pairwise iterative, optimization-based approaches have been extensively studied in medical image registration (Hill et al., 2001; Oliveira and Tavares, 2014). These methods employ a variety of similarity functions, types of deformation, transformation constraints or regularization strategies, and optimization techniques. Intensity-based similarity criteria are most often used, such as mean-squared error (MSE) or normalized cross correlation for registering images of the same modality (Avants et al., 2009, 2008a; Hermosillo et al., 2002). For registering image pairs from different modalities, statistical measures like mutual information or contrast-invariant features like MIND are popular (Heinrich et al., 2012; Hermosillo et al., 2002; Hoffmann et al., 2021; Mattes et al., 2003; Viola and Wells III, 1997).

Another registration paradigm first detects features or keypoints in the images, and then establishes their correspondence. This approach often involves hand-crafted features (Tuytelaars and Mikolajczyk, 2008), features extracted from curvature of contours (Rosenfeld and Thurston, 1971), image intensity (Förstner and Gülch, 1987; Harris et al., 1988), color information (Montesinos et al., 1998; Van de Weijer et al., 2005), or segmented regions (Matas et al., 2004; Wachinger et al., 2018). Features can be also obtained so that they are invariant to viewpoints (Bay et al., 2006; Brown et al., 2005; Lowe, 2004; Toews et al., 2013). These algorithms then optimize

similarity functions based on these features over the space of transformations (Chui and Rangarajan, 2003; Hill et al., 2001). This strategy is sensitive to the quality of the keypoints and often suffer in the presence of substantial contrast and/or color variation (Verdie et al., 2015).

Learning-based Methods. In learning-based image registration, supervision can be provided through ground-truth transformations, either synthesized or computed by classical methods (Cao et al., 2018; Dosovitskiy et al., 2015; Eppenhof and Pluim, 2018; Lee et al., 2019a; Uzunova et al., 2017; Yang et al., 2017). Unsupervised strategies use loss functions similar to those employed in classical methods (Balakrishnan et al., 2019; Dalca et al., 2019; de Vos et al., 2019; Fan et al., 2018; Krebs et al., 2019; Qin et al., 2019; Wu et al., 2015; Hoopes et al., 2021). Weakly supervised models employ (additional) landmarks or labels to guide training (Balakrishnan et al., 2019; Fan et al., 2019; Hu et al., 2018a,b).

Recent learning-based methods compute image features or keypoints (Ma et al., 2021) that can be used for image recognition, retrieval, or registration. Learning useful features or keypoints can be done with supervision (Verdie et al., 2015; Yi et al., 2016, 2018), self-supervision (DeTone et al., 2018; Liu et al., 2021) or without supervision (Barroso-Laguna et al., 2019; Lenc and Vedaldi, 2016; Ono et al., 2018). Finding correspondences between pairs of images usually involves identifying the learned features which are most similar between

the pair. In contrast, our method uses a network which extract/generates keypoints directly from the image. The keypoints between the moving and fixed image are corresponding (i.e., matched) by construction, and we optimize these corresponding keypoints directly for the registration task (and not using any intermediate keypoint supervision).

Learning-based methods for multi-modal registration are of great practical utility and often-studied in the literature. Most works require, in addition to the moving and fixed image, a corresponding image in a standard space which can be compared and which drives the alignment, usually in the form of segmentations. Zhang et al. (2022) address multi-modal retinal images and handle multi-modality by transforming each image to a standard grayscale image via vessel segmentation. A standard feature detection and description procedure is used to find correspondences from these standard images. Other works Song et al. (2022) rely on segmentations from ultrasound and magnetic resonance images to align them. Obtaining these segmentations may be costly, add additional computational complexity to the registration procedure, or be specific to the anatomies/modalities in question. In contrast, our method can be applied generally to any registration problem. In addition, we present a variant of our model which only relies on the images themselves during training. In our experiments, we find that this variant outperforms state-of-the-art baselines while also performing comparably to a variant of our model which leverages segmentations.

Hyperparameter-Agnostic Methods. A recent line of work focuses on making the model agnostic to the hyperparameter which weights the smoothness prior (Hoopes et al., 2021; Mok and Chung, 2021; Wang et al., 2022). These models accept the image pair and hyperparameter as input and modulate the network according to the hyperparameter, either by passing the hyperparameter as input to a hypernetwork which outputs the weights of the main registration network (Hoopes et al., 2021; Wang et al., 2022), or by performing instance normalization on the intermediate feature maps (Mok and Chung, 2021). In this work, we propose an alternative strategy to efficiently produce hyperparameter-specific registration results directly from learned keypoints. In particular, our approach does not require a hypernetwork architecture or any modula-

tion of the architecture itself.

3. Differentiable, Closed-Form Coordinate Transformations

Notation: In the following sections, column vectors are lower-case bolded and matrices are upper-case bolded. D -dimensional coordinates are represented as column vectors, i.e. $\mathbf{p} \in \mathbb{R}^D$. D is typically 2 or 3. $\tilde{\mathbf{p}}$ denotes \mathbf{p} in homogeneous coordinates, i.e. $\tilde{\mathbf{p}} = [\mathbf{p}, 1]^T$. Superscripts in parentheses $\mathbf{p}^{(i)}$ index over separate instances of \mathbf{p} (e.g. in a dataset), whereas subscripts \mathbf{p}_i denotes the i 'th element of \mathbf{p} .

We present two parametric transformation families that can be derived in closed-form, from corresponding keypoint pairs. Suppose we have a set of N corresponding keypoint pairs $\{(\mathbf{p}^{(i)}, \mathbf{q}^{(i)})\}_{i=1}^N$, where $\mathbf{p}^{(i)}, \mathbf{q}^{(i)} \in \mathbb{R}^D$ and $N > D$. For convenience, let $\mathbf{P} := [\mathbf{p}^{(1)} \dots \mathbf{p}^{(N)}] \in \mathbb{R}^{D \times N}$, and similarly for $\tilde{\mathbf{P}}$ and \mathbf{Q} . Define $\mathcal{T}_\theta : \mathbb{R}^D \rightarrow \mathbb{R}^D$ as a family of coordinate transformations, where $\theta \in \Theta$ are parameters of the transformation.

3.1. Affine

Affine transformations are represented as a matrix multiplication of $\mathbf{A} \in \mathbb{R}^{D \times (D+1)}$ with a coordinate in homogeneous form:

$$\mathcal{T}_\theta(\mathbf{p}) = \mathbf{A}\tilde{\mathbf{p}}, \quad (1)$$

where the parameter set is the elements of the matrix, $\theta = \{\mathbf{A}\}$.

Given N corresponding keypoint pairs, there exists a differentiable, closed-form expression for an affine transformation that aligns the keypoints:

$$\theta^*(\mathbf{P}, \mathbf{Q}) := \arg \min_{\theta} \sum_{i=1}^N (\mathbf{A}\tilde{\mathbf{p}}^{(i)} - \mathbf{q}^{(i)})^2 \quad (2)$$

$$= \mathbf{Q}\tilde{\mathbf{P}}^T (\tilde{\mathbf{P}}\tilde{\mathbf{P}}^T)^{-1}. \quad (3)$$

A derivation is provided in the Appendix. This is the least-squares solution to an overdetermined system, and thus in practice the points will not be exactly matched due to the restrictive nature of the affine transformation. This restrictiveness may be alleviated or removed by choosing a transformation family with additional degrees of freedom, as we detail next.

3.2. Thin-Plate Spline

The application of the thin-plate spline (TPS) interpolant to modeling coordinate transformations yields a parametric, non-rigid deformation model which admits a closed-form expression for the solution that interpolates a set of corresponding keypoints (Bookstein, 1989; Donato and Belongie, 2002; Rohr et al., 2001). This provides additional degrees of freedom over the affine family of transformations, while also subsuming it as a special case.

For the d 'th dimension, the TPS interpolant $\mathcal{T}_{\theta_d} : \mathbb{R}^D \rightarrow \mathbb{R}$ takes the following form:

$$\mathcal{T}_{\theta_d}(\mathbf{p}) = (\mathbf{a}_d)^T \tilde{\mathbf{p}} + \sum_{i=1}^N w_{i,d} U(\|\mathbf{p}^{(i)} - \mathbf{p}\|_2), \quad (4)$$

where $\mathbf{a}_d \in \mathbb{R}^{D+1}$ and $\{w_{i,d}\}$ constitute the transformation parameters θ_d and $U(r) = r^2 \ln(r)$. We define $\mathbf{A} \in \mathbb{R}^{(D+1) \times D}$ and $\mathbf{W} \in \mathbb{R}^{N \times D}$ as the collection of all the parameters for $d = 1, \dots, D$. Then, the parameter set is $\theta = \{\mathbf{A}, \mathbf{W}\}$.

This form of \mathcal{T} minimizes the *bending energy*:

$$I_{\mathcal{T}} = \int_{\mathbb{R}^D} \|\nabla^2 \mathcal{T}\|_F^2 d\mathbf{p}_1 \dots d\mathbf{p}_D, \quad (5)$$

where $\|\cdot\|_F$ is the Frobenius norm and $\nabla^2 \mathcal{T}$ is the matrix of second-order partial derivatives of \mathcal{T} . For each θ_d , we impose interpolation conditions $\mathcal{T}_{\theta_d}(\mathbf{p}^{(i)}) = \mathbf{q}_d^{(i)}$ and enforce \mathcal{T} to have square-integrable second derivatives:

$$\sum_{i=1}^N w_{i,d} = 0 \quad \text{and} \quad \sum_{i=1}^N w_{i,d} \mathbf{p}_d = 0 \quad \forall d \in \{1, \dots, D\}. \quad (6)$$

Given these conditions, the following system of linear equations solves for θ :

$$\Psi \theta := \begin{bmatrix} \mathbf{K} & \mathbf{L} \\ \mathbf{L}^T & \mathbf{O} \end{bmatrix} \begin{bmatrix} \mathbf{W} \\ \mathbf{A} \end{bmatrix} = \begin{bmatrix} \mathbf{Q}^T \\ \mathbf{O} \end{bmatrix} := \mathbf{Z}. \quad (7)$$

Here, $\mathbf{K} \in \mathbb{R}^{N \times N}$ where $K_{ij} = U(\|\mathbf{p}^{(i)} - \mathbf{p}^{(j)}\|_2)$, $\mathbf{L} \in \mathbb{R}^{N \times (D+1)}$ where the i 'th row is $(\tilde{\mathbf{p}}^{(i)})^T$, and \mathbf{O} is a matrix of zeros with appropriate dimensions. Thus,

$$\theta^*(\mathbf{P}, \mathbf{Q}) := \Psi^{-1} \mathbf{Z}. \quad (8)$$

Solving for θ^* is a differentiable operation.

The interpolation conditions can be relaxed (e.g. under the presence of noise) by introducing a regularization term:

$$\arg \min_{\theta_d} \sum_{i=1}^N (\mathcal{T}_{\theta_d}(\mathbf{p}^{(i)}) - \mathbf{q}_d^{(i)})^2 + \lambda I_{\mathcal{T}} \quad (9)$$

where $\lambda > 0$ is a hyperparameter that controls the strength of regularization. As λ approaches ∞ , the optimal \mathcal{T} approaches the affine case (i.e. zero bending energy). This formulation can be solved exactly by replacing \mathbf{K} with $\mathbf{K} + \lambda \mathbf{I}$ in Eq. (7). Importantly, θ and the optimal $\theta^*(\mathbf{P}, \mathbf{Q})$ exhibits a dependence on λ .

4. KeyMorph

Let $(\mathbf{x}_m, \mathbf{x}_f)$ be moving (source) and fixed (target) image¹ pairs, possibly of different contrasts or modalities. Additionally, we denote by \mathcal{T}_{θ} a parametric coordinate transformation with parameters θ , such as those discussed in Section 3. Our goal is to find the optimal transformation \mathcal{T}_{θ^*} such that the registered image $\mathbf{x}_r = \mathbf{x}_m \circ \mathcal{T}_{\theta^*}$ aligns with the fixed image \mathbf{x}_f , where \circ denotes the spatial transformation of an image.

KeyMorph derives the optimal θ^* by detecting N *corresponding keypoints* $\mathbf{P}, \mathbf{Q} \in \mathbb{R}^{D \times N}$ from \mathbf{x}_m and \mathbf{x}_f , respectively. Furthermore, by choosing a transformation family whose optimal parameters admits a closed-form and differentiable solution $\theta^*(\mathbf{Q}, \mathbf{P})$ as a function of these keypoints, the keypoints themselves are learned by a neural network in an end-to-end fashion².

We define a CNN as f_w with parameters w , which detects N corresponding keypoints from both the moving and fixed image: $\mathbf{P} = f_w(\mathbf{x}_m)$ and $\mathbf{Q} = f_w(\mathbf{x}_f)$. Supposing we have a dataset of such pairs, the general KeyMorph objective is:

$$\arg \min_w \mathbb{E}_{(\mathbf{x}_m, \mathbf{x}_f)} \mathcal{L}_{sim}(\mathbf{x}_m \circ \mathcal{T}_{\theta^*}, \mathbf{x}_f) \quad (10)$$

where $\theta^* = \theta^*(f_w(\mathbf{x}_f), f_w(\mathbf{x}_m))$

¹Although we consider 3D volumes in this work, KeyMorph is agnostic to the number of dimensions. The terms “image” and “volume” are used interchangeably.

²Note that the arguments of θ^* are switched (i.e. the transformation \mathcal{T} is applied to the “fixed” keypoints \mathbf{Q}), because we are seeking a transformation that takes us from fixed image coordinates to moving image coordinates in order to resample the moving image.

where $\mathcal{L}_{sim}(\cdot, \cdot)$ measures image similarity between its two inputs. Fig. 2 depicts the proposed model architecture. The closed-form optimal solution θ^* can depend on a hyperparameter λ , such as in TPS, which can be set to a constant or sampled from a distribution $\lambda \sim p(\lambda)$ during training. Once the model is trained, at test (inference) time, one can swap the transformation with a different model (e.g. replace affine with TPS) or use a different hyperparameter value, which would yield a different alignment based on the same keypoints.

There are several advantages to our formulation over prior learning-based methods. 1) The closed-form solution is not sensitive to the relative placement of the keypoints. Thus, robustness to large misalignments is achieved if the CNN is equivariant with respect to input image deformation. Intuitively, this is an easier task for the network to learn as compared to having to learn both correspondences and the transformation directly from the image pairs. 2) Visualizing the keypoints enables the user to interpret what parts of the image is driving the alignment. In contrast to deformation fields which encode correspondence and transformation in a dense velocity space, keypoints are easily visualized and overlaid on the image space. Furthermore, the keypoints are guaranteed to be anatomically consistent by construction; as a result, they can be used to understand and verify model behavior, or leveraged for downstream tasks. 3) With careful design of the keypoint detection network (see Section 4.1), translational-equivariance can be achieved. 4) Once the model is trained, different coordinate transformations or different transformation hyperparameters can be used to generate a dense set of registrations at test-time; the controllable nature of this framework enables the user to select the preferred registration. Note that these registrations require no modulation of the CNN to produce.

4.1. Keypoint Detector Architecture

KeyMorph is a framework that can leverage any deep learning-based keypoint detector (Ma et al., 2021; DeTone et al., 2018; Barroso-Laguna et al., 2019). In this work, we are interested in preserving translation equivariance; to this end, we leverage a center-of-mass (CoM) layer (Ma et al., 2020; Sofka et al., 2017) as the final layer, which computes the center-of-mass for each of the N activation maps. This specialized layer is (approximately)

translationally-equivariant and enables precise localization. Our architecture backbone consists of convolutional layers followed by instance normalization (Ulyanov et al., 2016), ReLU activation, and 2x downsampling via strided convolution, as shown in Fig. 2.

4.2. Training and Model Variants

We present two training strategies corresponding to two model variants of KeyMorph. For both variants, we apply random affine transformations to the moving image \mathbf{x}_m as an augmentation strategy, the details of which are in Section 5.3.

4.2.1. Supervised

In what we refer to as the “supervised” setting, the model may exploit segmentations during training. In this work, we use soft-Dice for \mathcal{L}_{sim} , which measures volume overlap of the moving and registered label maps (Balakrishnan et al., 2019; Hoffmann et al., 2021; Hu et al., 2018a). Note that label maps are only used to compute the loss and are not an input to the model.

4.2.2. Unsupervised

In what we refer to as the “unsupervised” setting, we assume we have access to intensity images only. Here, \mathcal{L}_{sim} is mean squared error (or MSE) on pixel intensity values and is computed only on *same-modality* image pairs.

To ensure that keypoints remain consistent across modalities, we add an additional loss that penalizes within-subject multi-modal (e.g. T1, T2, PD-weighted MRI) keypoint deviation. Thus, in the unsupervised setting, we alternate between mini-batches containing multi-subject uni-modal image pairs (where pixel MSE is the loss function as in Eq.(10)) and the following same-subject multi-modal image pairs (where keypoint MSE is the loss function):

$$\mathcal{L}_u(w) = \mathbb{E}_{(\mathbf{x}_1, \mathbf{x}_2)} \|f_w(\mathbf{x}_1) - f_w(\mathbf{x}_2)\|_F, \quad (11)$$

where $(\mathbf{x}_1, \mathbf{x}_2)$ is a pair of images from the same subject with different modality. This is equivalent to minimizing the sum of the losses with equal weight, which we found to work well in practice. We apply random affine transformations to the same-subject multi-modal image pairs as an augmentation strategy.

<i>Model</i>	<i>CPU Time (s)</i>	<i>GPU Time (s)</i>
ANTs-Aff	50.59±1.18	-
ANTs-Syn	52.70±0.72	-
DLIR	1.49±0.09	0.02±0.001
KM-Aff (Ours)	2.61±0.53	0.09±0.001
KM-TPS (Ours)	4.29±0.17	0.23±0.009

Table 1: Average computation time across different models during testing.

Note that, contrary to other multi-modal registration methods, \mathcal{L}_{sim} is set to MSE for both uni-modal and multi-modal training.

4.3. Self-supervised Pretraining

We employ the following self-supervised pre-training strategy to aid in keypoint detector initialization. Consider a single subject and its set of aligned different-modality scans $\{\mathbf{x}^{(i)}\}$. We pick a random set of keypoints \mathbf{P}_0 by sampling uniformly over the image coordinate grid. In each mini-batch, we apply random affine and nonlinear transformations to $\mathbf{x}^{(i)}$ and \mathbf{P}_0 , and minimize the following keypoint loss:

$$\arg \min_w \sum_i \mathbb{E}_{\mathbf{A}, \phi} \left\| \phi(\mathbf{A}\mathbf{P}_0) - f_w(\mathbf{x}^{(i)} \circ \mathbf{A} \circ \phi) \right\|_2^2. \quad (12)$$

Here, \mathbf{A} is an affine transformation drawn from a uniform distribution over the parameter space. ϕ is a nonlinear transformation generated by integrating a random stationary velocity field (see Ashburner (2007); Dalca et al. (2018); Hoffmann et al. (2021) for more details).

Empirically, we find that this relatively lightweight pre-training step is necessary to encourage the keypoints to spread out across the image. Without it, the training dynamics suffer due to being stuck in a local minimum where the keypoints cluster tightly in the middle of the image, leading to suboptimal solutions.

5. Experimental Setup

5.1. Dataset

We experiment on the IXI brain MRI dataset³. Each subject has T1, T2, and PD-weighted 3D MRI scans in

spatial alignment. We perform the following standard pre-processing steps: resampling to 1mm isotropic, rescaling intensity values between $[0, 1]$, and padding to 256^3 image size. We partition the 577 total subjects into sets of 427, 50, and 100 for training, validation, and testing, respectively. We perform standard skull stripping (Kleesiek et al., 2016) on all images.

We use a pre-trained and validated SynthSeg model (Billot et al., 2020) to automatically delineate 23 regions of interest (ROIs)⁴. These segmentations were used for training a subset of (supervised) models, as described below. Furthermore, all performance evaluations were based on examining the overlap of ROIs in the test images.

5.1.1. Test-time Performance Evaluation

We use each testing subject as a moving volume \mathbf{x}_m , paired with another random test subject treated as a fixed volume \mathbf{x}_f . For all test volumes, we use 23-label segmentation maps to quantify alignment. We simulate different degrees of misalignment by transforming \mathbf{x}_m using rotation. 1 to 3 axes are chosen randomly and a uniform random rotation is applied up to a given degree. We use the predicted transformation to resample the moved segmentation labels on the fixed image grid. We quantify alignment quality and properties of the transformation using Dice overlap score, Hausdorff distance, standard deviation of the Jacobian determinant, and percentage of voxels less than 0 in the Jacobian determinant.

We perform registration across all combinations of available modalities (registering T1 to T1, T1 to T2, etc). All pairings and amount of transformations are kept the same across the registration experiments.

5.2. Baselines

Advanced Normalizing Tools (ANTs) is a widely-used software package which is state-of-the-art for medical image registration (Avants et al., 2009). For the affine model, we use “TRSAA” affine implementation (ANTs-Aff), which consist of translation, rigid, similarity

³<https://brain-development.org/ixi-dataset/>

⁴ROIs were pallidum, amygdala, caudate, cerebral cortex, hippocampus, thalamus, putamen, white matter, cerebellar cortex, ventricle, cerebral white matter, and brainstem.

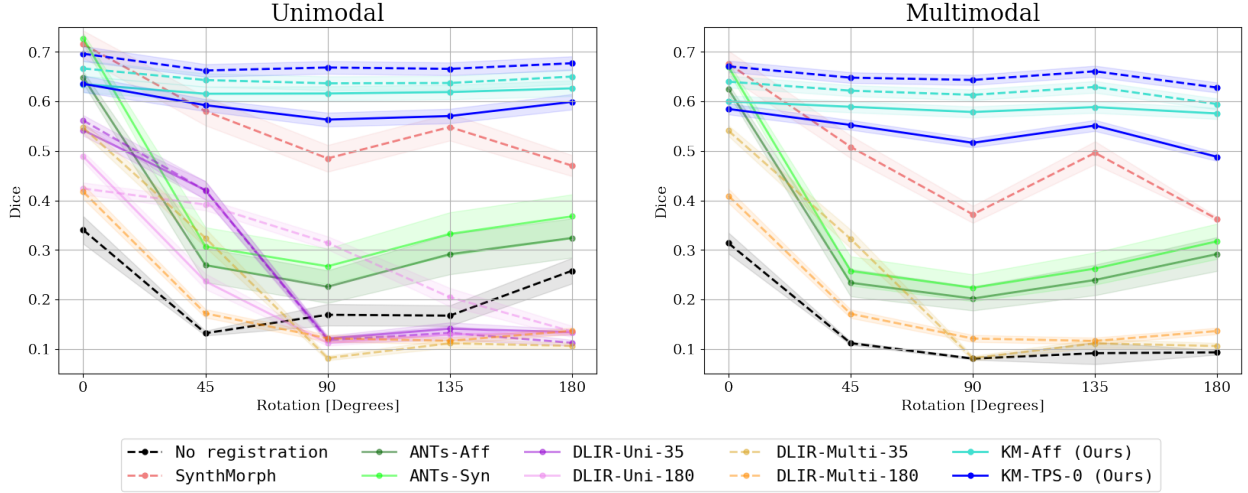


Figure 3: KeyMorph and baseline performance across varying rotation angle. The Dice score is averaged for all test subjects and brain anatomical regions. Solid lines denote unsupervised models and dashed lines denote supervised models (i.e. with or without ground-truth segmentations). Shaded regions denote standard deviation.

and two affine transformation steps. The volumes are registered successively at three different resolutions: 0.25x, 0.5x and finally at full resolution. At 0.25x and 0.5x resolution, Gaussian smoothing with σ of two and one voxels is applied, respectively. For non-linear registration, we use “SynRA” (ANTs-Syn), which consists of an initial rigid and affine alignment step followed by Symmetric Normalization (Avants et al., 2008b). For both ANTs-Aff and ANTs-Syn, we use the ANTs affine initializer at large deformation, which conducts a grid search over a range of rotations and translations to help find a good initialization. Finally, we used mutual information as the similarity metric for both models, which is suitable for registering images with different contrasts.

Deep Learning for Image Registration (DLIR) is a recent learning-based method that supports affine and deformable image registration (de Vos et al., 2019), and which we believe is representative of many deep learning models which leverage a Spatial Transformer Network (Jaderberg et al., 2015) (STN). STNs were originally used to improve class prediction accuracy and has since become the backbone of many subsequent works in image registration (de Vos et al., 2017; Lee et al., 2019b; Balakrishnan et al., 2019). For a direct comparison, we used the same backbone architecture as KeyMorph replac-

ing the center-of-mass layer with a fully-connected (FC) layer which outputs 12 parameters for the 3D affine transformation.⁵

For all DLIR training, we use the following ranges for random augmentations: translations $[-15, 15]$ voxels, scaling factor $[0.8, 1.2]$, and shear $[-0.1, 0.1]$. We find that DLIR often cannot register image pairs with large misalignments, especially under large rotation misalignment. We alleviate this by using more aggressive rotation augmentation during training. We consider two different amounts of rotation for the training of DLIR: maximum $\pm 35^\circ$ or $\pm 180^\circ$. We use the same loss function and training scheme as we used for KeyMorph. We trained separate DLIR models for each modality as it produces better results than training DLIR across modalities with mutual information. We also trained *supervised* modality-specific and multi-modal DLIR models using a soft-Dice loss computed on the aligned segmentation maps (Lee et al., 2019a).

Altogether, we implement six different DLIR variants. The naming scheme follows the convention

⁵We used instance norms for multimodal DLIR and batch norms for unimodal DLIR, which we found to work well in practice.

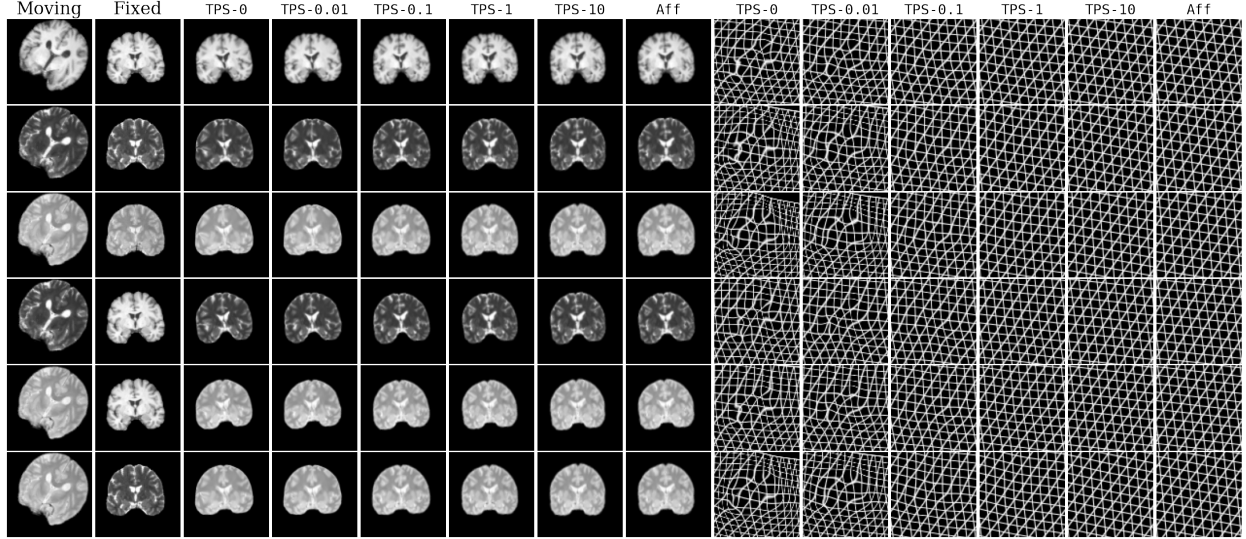


Figure 4: Representative registration results on different volumes from a pair of subjects, for unsupervised KM variants. Registered images are performed for different TPS λ 's and affine transformations. Deformed grids are depicted.

DLIR- $\langle \text{mod} \rangle$ - $\langle \text{degree} \rangle$, where $\langle \text{mod} \rangle$ denotes whether the model was trained on a single (Uni) or multiple (Multi) modalities and $\langle \text{degree} \rangle$ denotes the maximum angle of rotation for augmentation. We train supervised and unsupervised versions of unimodal DLIR, and only train supervised versions of multimodal DLIR.

SynthMorph is a recently-proposed deep learning model which achieves agnosticism to modality/contrast by leveraging a generative strategy for synthesizing diverse images, thereby supporting multi-modal registration (Hoffmann et al., 2022). Like DLIR, it accepts as input the moving and fixed images but outputs a dense deformation field instead of global affine parameters, which is a common strategy in many well-performing registration models (Balakrishnan et al., 2019). However, a crucial assumption of many of these models is that the image pair must first be affine registered. Although KeyMorph does not have this assumption, we follow this required step to maximize the performance of SynthMorph. Following their suggested pre-registration method, we first affine-register each image pair using `mri-robust-register`⁶ from the Freesurfer pack-

age (Fischl, 2012).

5.3. Model and Training Details

We train six variants of KeyMorph (KM) corresponding to six *pre-determined* transformations: 1 model using an affine transformation and 5 models using a TPS transformation with $\lambda \in \{0, 0.01, 0.1, 1, 10\}$. We refer to these models as KM-Aff and KM-TPS- λ . Additionally, we train a variant using a TPS transformation where λ is sampled *stochastically* during training from a log-uniform distribution $p(\lambda) = \text{LogUnif}(0, 10)$. We refer to this model as KM-LogUnif. We used $N = 128$ keypoints throughout our experiments, and analyze the effect of changing this number in Section 6.2.

For all models, we used a batch size of 1 image pair and the Adam optimizer (Kingma and Ba, 2017) for training. The following uniformly-sampled augmentations were applied to the moving image across all dimensions during training: rotations $[-180^\circ, +180^\circ]$, translations $[-15, 15]$ voxels, scaling factor $[0.8, 1.2]$, and shear $[-0.1, 0.1]$. Note that this is the same augmentation strategy as DLIR variants with $[-180^\circ, +180^\circ]$ rotation aug-

⁶https://surfer.nmr.mgh.harvard.edu/fswiki/mri_robust_register

`robust_register`

mentation. All training and GPU testing was performed on a machine equipped with an Intel Xeon Gold 6126 processor and an Nvidia Titan RTX GPU. CPU testing was performed on a machine equipped with an AMD EPYC 7642 48-Core Processor. All models were implemented in Pytorch.

6. Results

6.1. Main Results

6.1.1. KeyMorph is robust to large misalignments

We analyze the performance of baselines and our proposed KeyMorph under conditions of large initial misalignments in terms of rotation. Fig. 3 plots overall Dice across rotation angle of the moving image for baselines and two variants of KeyMorph: KM-Aff and KM-TPS-0.

We find that all DLIR models suffer substantially as the rotation angle increases. Training with aggressive augmentation increases performance for test pairs with large misalignments, but reduces the accuracy for those with smaller misalignments. Using supervision (dashed DLIR lines) leads to improved accuracy. For unimodal registration, the DLIR model that was trained with all modalities (DLIR-Multi) did not produce better accuracy than a model that was trained with each modality separately. ANTs yields excellent results when the initial misalignment is small (e.g. near 0 degrees of rotation). However, the accuracy drops substantially when the misalignment exceeds this range.

In contrast to these models, KeyMorph variants performed well across all types of transformations and ranges, with only marginal drops in accuracy in large misalignments. In the case where we have access to ROIs during training, we find that KeyMorph trained with Dice outperforms all models except ANTs-Syn. However, the unsupervised variant trained with MSE still yields excellent accuracy across all settings and is only minimally suboptimal compared to its supervised counterpart.

The supervised variant of KM-TPS-0 outperforms its KM-Aff counterpart, whereas the opposite is true in unsupervised variants; we attribute this to the increased expressivity of low λ in the TPS transformation overfitting to the MSE loss function at the cost of Dice performance (empirically, we observe that low λ achieves better performance in terms of MSE compared to high λ for unsupervised variants, see Fig. 13).

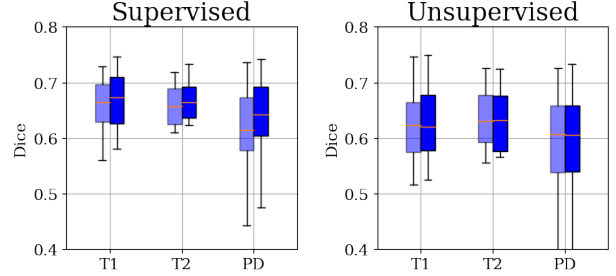


Figure 5: Multimodal KeyMorph vs. unimodal KeyMorph models trained on individual modalities. Supervised and unsupervised.

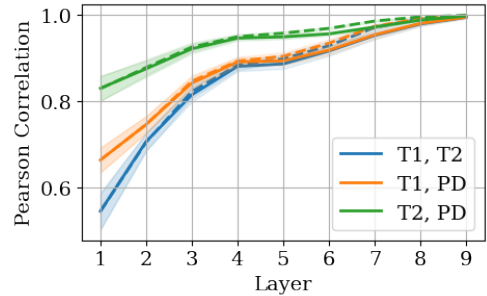


Figure 6: Pearson correlation of feature maps across layers of trained unsupervised (solid) and supervised (dashed) model. Correlation is computed between each combination of (T1, T2, and PD) multi-modal volume pairs, for a fixed subject. Final value is average across subjects, and shaded regions denote standard deviation.

We provide qualitative results in Fig. 4, and compare the computational time across different models in Table 1. A comprehensive table of all methods and initial misalignments separated by modality are in Table B.3. Additional metrics including Hausdorff distance and Jacobian-based metrics are presented in Fig. B.16. Qualitative registrations for all models is provided in Fig. B.17 and B.18. Overall, the KeyMorph (KM) variants outperform other learning-based baselines, and KeyMorph performs comparably or often better (at large misalignments) than the state-of-the-art ANTs registration, while requiring substantially less runtime.

6.1.2. KeyMorph supports multi-modal registration

To test the efficacy of the multi-modal training strategy of KeyMorph, we compare the performance of a single KeyMorph model trained with our multi-modal strat-

egy against 3 separate KeyMorph models on 3 different modalities. Results are shown in Fig. 5, which demonstrate that the multi-modal training strategy achieves comparable results to the modality-specific models.

We hypothesize that in order to remain consistent across modalities, the keypoint detector must learn to be invariant to contrasts. To test this, we plot the Pearson correlation of feature maps for multi-modal image pairs, across the layers of the CNN (see Fig. 6). For a given subject and a given layer, we extract the intermediate feature maps for the 3 modalities and compute the Pearson correlation between every pair of modalities. Then, we average across all subjects, for each layer. We observe that the correlation increases with the depth of the network, indicating that the features become more invariant to the input modality at deeper layers.

6.1.3. CoM layer outperforms FC layer

We test whether the translation-equivariance properties of the CoM layer leads to improved registration performance. Fig. 7 shows results on KeyMorph variants trained with the CoM layer vs. an FC layer. We see that the CoM outperforms FC over the range of transformations.

6.1.4. Multiple registrations at test-time provide nuanced predictions

Given learned keypoints, KeyMorph can generate a dense set of registrations at test-time corresponding to different transformations. It follows that the quality of registrations is subject to whether a single set of learned keypoints can perform well across many different transformations.

To this end, we analyze the ability of learned keypoints to generalize to new transformation hyperparameters. In Fig. 8, each solid line is generated by taking the corresponding model and evaluating it on different transformations at test-time. The dashed “Matched” line denotes the performance of multiple models trained on its corresponding transformation, and is an upper-bound on performance. As expected, we notice that KM-TPS-0 performs well at low λ values and vice versa for KM-Aff. By comparison, KM-LogUnif performs comparably to these fixed models at the endpoints, and outperforms both near the middle region (i.e. $\lambda \in [0.1, 10]$). Overall, it performs comparably to the upper-bound across all transformations. We conclude that sampling from a hyperparam-

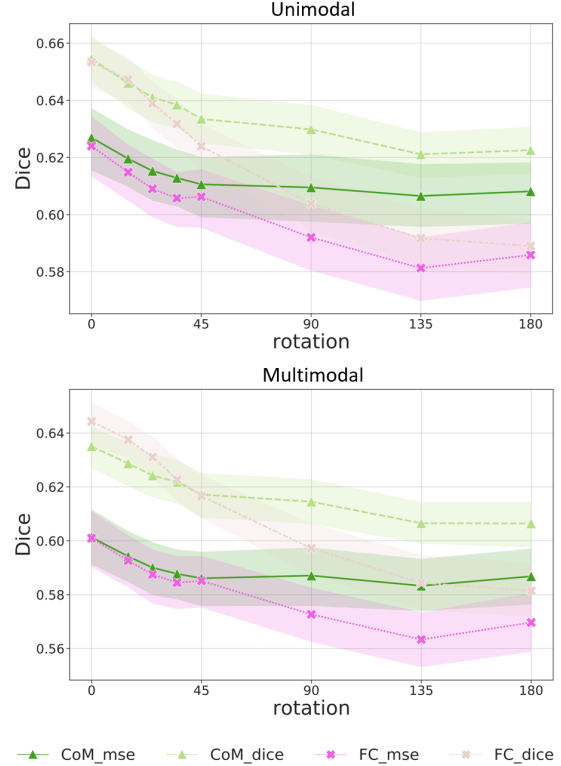


Figure 7: Performance comparison between KeyMorph models that uses center-of-mass (CoM) and fully connected (FC) layers to predict keypoints. The suffix `mse` and `dice` represent the unsupervised and supervised version of KeyMorph, respectively. Shaded regions denote standard deviation.

eter distribution allows the learned keypoints to be useful for a range of transformations, and that a single trained model can be used in lieu of multiple trained models on single settings of the hyperparameters.

To demonstrate a downstream utility that multiple optimal registrations afford (and following Hoopes et al. (2021)), we study the relationship between regional Dice scores and the hyperparameter value. Fig. 9 plots Dice scores achieved by KM-LogUnif for several ROIs across different values of λ , densely sampled in $[0, 10]$. We observe that the optimal Dice score for a given ROI occurs at different λ values, and furthermore that the profiles of these curves can be quite different. The upshot is that since computing registrations with different λ values is efficient, an end user can quickly interrogate many optimal registra-

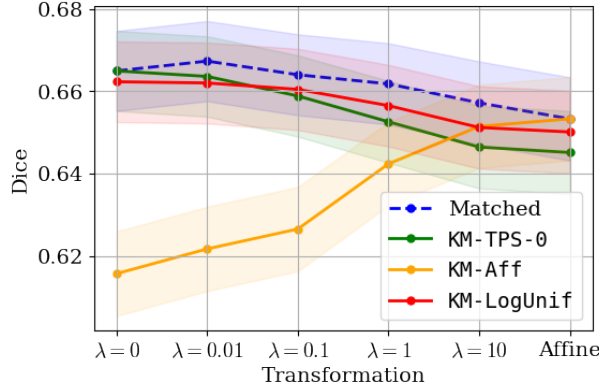


Figure 8: Dice performance over transformation variants. Solid lines are single, pretrained models evaluated on all transformations at test-time. Dashed blue line is multiple, pretrained models on matched transformation at test-time, which is an upper-bound on performance. Shaded regions denote standard deviation.

tions, each of which can be optimal for a different ROI.

6.1.5. KeyMorph can be made robust to noise

We explore whether KeyMorph can be made robust to noise factors like bias fields and random Gaussian noise through data augmentation during training. For random Gaussian noise, we uniformly sample the noise variance in $[0, 0.25]$. For bias field augmentation, we randomly sample the maximum magnitude of polynomial coefficients uniformly in $[0, 0.5]$. We evaluate the models on test subjects over the same range of noise and bias field parameters. Fig. 10 shows that the model can achieve adequate robustness by applying augmentations during training.

6.2. Keypoint Analysis

6.2.1. Visualizing keypoints

In contrast to existing models that compute the transformation parameters using a “black-box” neural network, we can investigate the keypoints that KeyMorph learns to drive the alignment. Fig. 11 depicts the keypoints for a moving and fixed subject pair across three slices of the volume and for 2 model variants, KM-TPS-0 and KM-TPS-10. The “Aligned” slices show both warped (dots) and fixed (crosses) points. As expected, we observe that a TPS transformation with $\lambda = 0$ exactly aligns

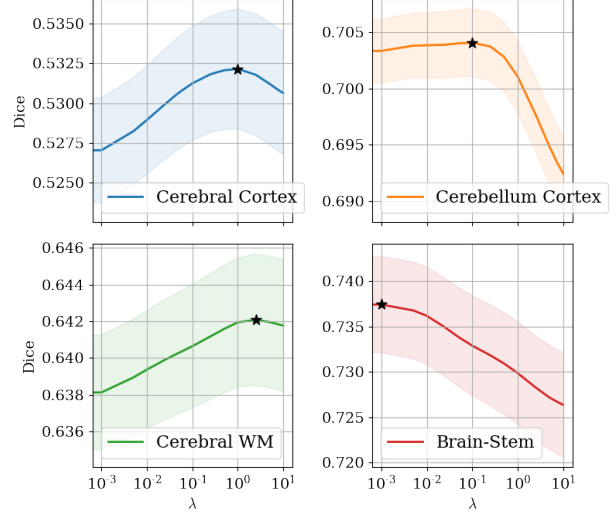


Figure 9: Dice performance over λ of KM-LogUnif separated by select ROIs. Stars denote maximum values. Shaded regions denote standard deviation.

the moving and fixed points; this exact interpolation is relaxed for $\lambda = 10$.

Keypoint locations are trained end-to-end without explicit annotations. Therefore, we are interested in the effect of the transformation on the learned keypoint locations. We observe that the KM-TPS-0 keypoints are more evenly distributed over the volume, whereas KM-TPS-10 keypoints have a higher degree of regularity and clustering. We attribute this to the fact that at low values of λ , each keypoint is a separate degree of freedom and can locally influence the deformation, so spreading out the points maximizes utility. On the other hand, TPS with $\lambda = 10$ is “affine-like” and has a higher restriction on its local deformation; thus, the model learns to cluster the points in certain regions, which are largely subcortical; we conjecture that the variability across subjects is low in these regions.

6.2.2. Keypoints are consistent across subject

We are interested in whether the model detects similar keypoint locations for volumes of the same subject but different modality, which we refer to as same-subject consistency. Note that same-subject consistency is explicitly optimized as a loss term in unsupervised variants. For

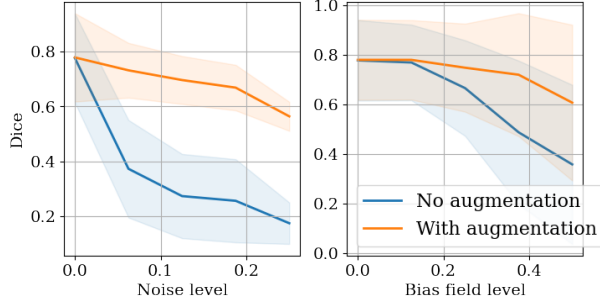


Figure 10: Comparison of KeyMorph performance trained with and without data augmentation (random Gaussian noise and bias field augmentation). KeyMorph achieves adequate robustness by applying augmentations during training. Shaded regions denote standard deviation.

supervised variants, consistency is implicit since multi-modal image pairs are presented during training.

In Fig. 12, we plot the average mean-squared-error (MSE) between the keypoints detected for 3 different combinations of modalities (T1 vs. T2, T1 vs. PD, and T2 vs. PD) across training. Bold lines denote standard supervised and unsupervised variants, and we observe that both models have decreasing keypoint deviation over training. Explicit encouragement of consistency in the unsupervised case leads to a higher degree of consistency than implicit encouragement in the supervised case.

In Fig. 12, we also investigate ablated versions of both supervised and unsupervised model variants, denoted by the corresponding color in faint lines. For unsupervised, we remove the explicit keypoint deviation loss. For supervised, we present only same-modality pairs during training. We notice that both ablations lead to worse results in terms of same-subject consistency.

6.2.3. Performance improves with increased keypoints

We examine the effect of the number of keypoints used for alignment across different transformations. We trained supervised KeyMorph model variants with 16, 32, 64, 128, 256, and 512 keypoints. Fig. 13 illustrates that while increasing the number of keypoints leads to a performance boost in general, the performance boost with more keypoints is higher for KM-TPS-0 than for KM-Aff models. We attribute this to the fact that transformations with higher degrees of nonlinearity benefit more from more degrees of freedom. For affine transformations, more key-

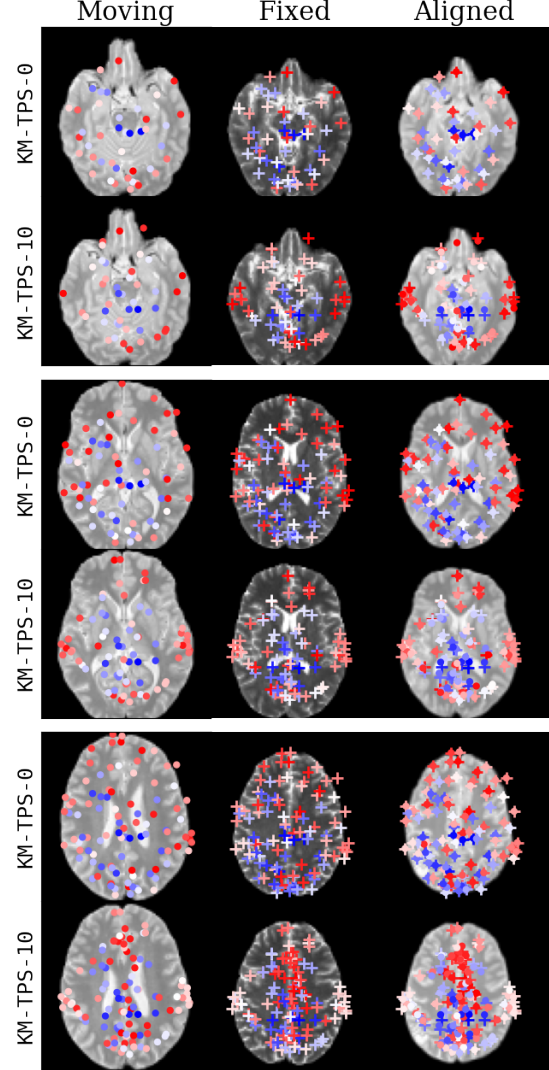


Figure 11: Keypoint visualization for a representative moving and fixed volume pair. For each slice, keypoints that are within 10 voxels of that slice are shown. Colors of keypoints reflect the distance of the keypoint to the visualized slice. For each slice, first row is KM-TPS-0, and second row is KM-TPS-10. Average distance between fixed (crosses) and aligned (dots) keypoints is 0 voxels for $\lambda = 0$ and 16.79 voxels for $\lambda = 10$.

points is largely redundant since the transformation applies globally. Indeed, we visually observe that higher numbers of keypoints leads to a higher amount of cluster-

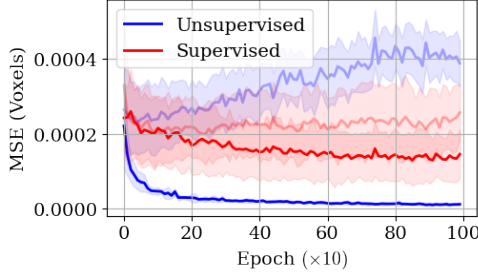


Figure 12: Same-subject keypoint deviation across training, in terms of MSE. Bold lines are standard MSE and Dice models as described in Section. 4.2. Faint lines are ablated versions of the corresponding model: faint blue is unsupervised training without the same-subject keypoint deviation loss term, and faint red is supervised training but presenting only same-modality pairs in Eq. (10). Shaded regions denote standard deviation.

ing and overlap of these keypoints for these transformation models (as can be gleaned from Fig. 11).

A current limitation of KeyMorph is the inability to train a higher number of keypoints due to computational constraints. We believe more keypoints for nonlinear transformations will lead to even better performance, as evidenced by the blue line in Fig. 13. Future research may investigate more memory-efficient keypoint architectures or leverage training strategies which admit a higher number of keypoints to be learned.

6.2.4. Keypoint extractor is repeatable

In KeyMorph, robustness to large misalignments is achieved if the keypoint extractor is equivariant with respect to input image deformation. To verify this, we apply a given transformation to both an image and its corresponding extracted keypoints. Then, we extract keypoints from the transformed image and compare the resulting keypoints with the directly transformed keypoints in terms of MSE. These results are plotted in Fig. 14. In particular, we observe that applying large transformations to the input image (e.g. 180 degree rotations, 15+ voxel translations, or 1.2x scaling) leads to only sub-voxel error in the predicted keypoints. Furthermore, our model readily admits the adoption of any variety of neural architectures which are equivariant under some class of transformations (see, for example, (Zhang, 2019)).

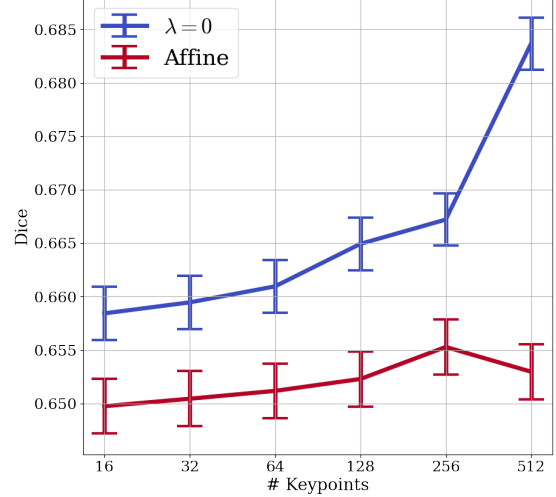


Figure 13: Performance for supervised models over varying number of keypoints. KM-TPS-0 (blue) has a higher boost in performance with more keypoints as compared to KM-Aff (red). Error bars denote standard deviation.

$\times 10^{-5}$	<i>T1 to T2</i>	<i>T2 to PD</i>	<i>T1 to PD</i>
<i>Same subject</i>	7.00 ± 3.29	4.87 ± 1.85	6.46 ± 3.75
<i>Different subject</i>	16.48 ± 6.35	15.99 ± 6.36	15.78 ± 6.43

Table 2: Subject-wise discriminability of predicted keypoints. Mean \pm standard deviation of Euclidean distance of keypoints between different modalities, split between same subject and different subject. Same subject keypoint distance is much lower, indicating subjects are discriminable on the basis of keypoints.

6.2.5. Subjects are discriminable via keypoints

If extracted keypoints are anatomically consistent, we would expect a subject to be discriminable on the basis of their keypoints (i.e. that their keypoints are “personalized”). Put another way, a subject’s keypoints extracted from modality 1 should be closest to its keypoints extracted from modality 2, compared to all other subjects’ keypoints extracted from modality 2 (and assuming all images are registered to a standardized space).

Fig. 15 shows error matrices between keypoints across all 100 subjects in the test set, for all 3 modality pairs (T1 to T2, T1 to PD, and T2 to PD). To generate these error matrices, we first extract keypoints from all test subjects for all 3 modalities (T1, T2, and PD). For each subject and a given modality, we perform affine registration of every

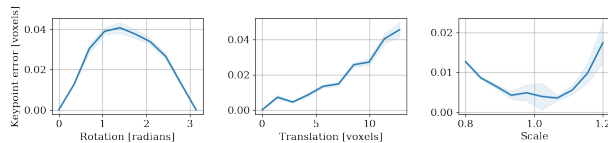


Figure 14: Repeatability of keypoints with respect to transformation. The given transformation is applied to both an image and its corresponding extracted keypoints. Then, keypoints are extracted from the transformed image and compared against the directly transformed keypoints in terms of MSE. In particular, we observe that applying large transformations to the input image (e.g. 180 degree rotations, 15+ voxel translations, or 1.2x scaling) leads to only sub-voxel error in the predicted keypoints. Shaded regions denote standard deviation.

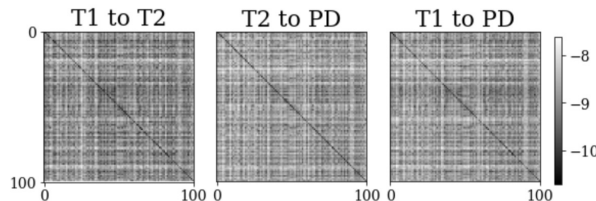


Figure 15: Log of keypoint error matrices across modality. Each row is the MSE of registered keypoints between one subject and every other subject. Matrix takes low value along the diagonal, indicating that keypoints extracted from the same subject are very similar across modalities; that is, a subject is discriminable on the basis of their extracted keypoints.

other subject (including itself) in a different modality to that first subject. Then, we compute the MSE of registered keypoints between that subject and every other subject, which constitutes a single row in the matrix. We observe that this matrix takes low value along the diagonal, indicating that keypoints extracted from the same subject are very similar across modalities; that is, a subject is discriminable on the basis of their extracted keypoints. In Table 2, we quantify this by averaging the errors over same subject and different subject (essentially, averaging over diagonal and non-diagonal entries).

7. Conclusion

We presented KeyMorph, a deep learning-based image registration method that uses corresponding keypoints to derive the optimal transformation that align the images. By unifying image registration and keypoint detection, we can train a model that finds matching keypoints useful

for aligning images. In addition, our method has the capability of having a higher degree of robustness to large misalignments, interpretability, controllability, and invariances inherent to the registration problem. We empirically demonstrate these capabilities on a large, real-world dataset of multi-modal brain MRI volumes.

Acknowledgments

This work was supported by NIH grants R01LM012719, R01AG053949, the NSF NeuroNex grant 1707312, and the NSF CAREER 1748377 grant (MS).

References

- Ashburner, J., 2007. A fast diffeomorphic image registration algorithm. *NeuroImage* 38, 95–113.
- Avants, B.B., Epstein, C.L., Grossman, M., Gee, J.C., 2008a. Symmetric diffeomorphic image registration with cross-correlation: evaluating automated labeling of elderly and neurodegenerative brain. *Medical image analysis* 12, 26–41.
- Avants, B.B., Epstein, C.L., Grossman, M., Gee, J.C., 2008b. Symmetric diffeomorphic image registration with cross-correlation: evaluating automated labeling of elderly and neurodegenerative brain. *Medical image analysis* 12, 26–41.
- Avants, B.B., Tustison, N., Song, G., 2009. Advanced normalization tools (ants). *Insight j* 2, 1–35.
- Balakrishnan, G., Zhao, A., Sabuncu, M.R., Guttag, J., Dalca, A.V., 2019. Voxelmorph: A learning framework for deformable medical image registration. *IEEE TMI* 38, 1788–1800.
- Barroso-Laguna, A., Riba, E., Ponsa, D., Mikolajczyk, K., 2019. Key. net: Keypoint detection by hand-crafted and learned cnn filters, in: *Proceedings of the IEEE/CVF International Conference on Computer Vision*, pp. 5836–5844.
- Bay, H., Tuytelaars, T., Van Gool, L., 2006. Surf: Speeded up robust features, in: *European conference on computer vision*, Springer. pp. 404–417.

- Billot, B., Greve, D., Van Leemput, K., Fischl, B., Iglesias, J.E., Dalca, A.V., 2020. A learning strategy for contrast-agnostic mri segmentation. *arXiv preprint arXiv:2003.01995*.
- Bookstein, F., 1989. Principal warps: thin-plate splines and the decomposition of deformations. *IEEE Transactions on Pattern Analysis and Machine Intelligence* 11, 567–585. doi:10.1109/34.24792.
- Brown, M., Szeliski, R., Winder, S., 2005. Multi-image matching using multi-scale oriented patches, in: 2005 IEEE Computer Society Conference on Computer Vision and Pattern Recognition (CVPR’05), IEEE. pp. 510–517.
- Cao, X., Yang, J., Zhang, J., Wang, Q., Yap, P.T., Shen, D., 2018. Deformable image registration using a cue-aware deep regression network. *IEEE Transactions on Biomedical Engineering* 65, 1900–1911.
- Chui, H., Rangarajan, A., 2003. A new point matching algorithm for non-rigid registration. *Computer Vision and Image Understanding* 89, 114–141.
- Dalca, A.V., Balakrishnan, G., Guttag, J., Sabuncu, M.R., 2018. Unsupervised learning for fast probabilistic diffeomorphic registration, in: *Medical Image Computing and Computer Assisted Intervention – MICCAI 2018*. Springer International Publishing, pp. 729–738.
- Dalca, A.V., Balakrishnan, G., Guttag, J., Sabuncu, M.R., 2019. Unsupervised learning of probabilistic diffeomorphic registration for images and surfaces. *Medical image analysis* 57, 226–236.
- DeTone, D., Malisiewicz, T., Rabinovich, A., 2018. Superpoint: Self-supervised interest point detection and description, in: *Proceedings of the IEEE conference on computer vision and pattern recognition workshops*, pp. 224–236.
- Donato, G., Belongie, S., 2002. Approximate thin plate spline mappings, in: Heyden, A., Sparr, G., Nielsen, M., Johansen, P. (Eds.), *Computer Vision — ECCV 2002*, Springer Berlin Heidelberg, Berlin, Heidelberg. pp. 21–31.
- Dosovitskiy, A., Fischer, P., Ilg, E., Hausser, P., Hazirbas, C., Golkov, V., Van Der Smagt, P., Cremers, D., Brox, T., 2015. FlowNet: Learning optical flow with convolutional networks, in: *Proceedings of the IEEE international conference on computer vision*, pp. 2758–2766.
- Eppenhof, K.A., Pluim, J.P., 2018. Pulmonary ct registration through supervised learning with convolutional neural networks. *IEEE transactions on medical imaging* 38, 1097–1105.
- Fan, J., Cao, X., Xue, Z., Yap, P.T., Shen, D., 2018. Adversarial similarity network for evaluating image alignment in deep learning based registration, 739–746.
- Fan, J., Cao, X., Yap, P.T., Shen, D., 2019. Birnet: Brain image registration using dual-supervised fully convolutional networks. *Medical image analysis* 54, 193–206.
- Fischl, B., 2012. Freesurfer. *NeuroImage* 62, 774–781.
- Förstner, W., Gülch, E., 1987. A fast operator for detection and precise location of distinct points, corners and centres of circular features, in: *Proc. ISPRS intercommission conference on fast processing of photogrammetric data*, Interlaken. pp. 281–305.
- Harris, C.G., Stephens, M., et al., 1988. A combined corner and edge detector., in: *Alvey vision conference*, Citeseer. pp. 10–5244.
- Heinrich, M.P., Jenkinson, M., Bhushan, M., Matin, T., Gleeson, F.V., Brady, M., Schnabel, J.A., 2012. Mind: Modality independent neighbourhood descriptor for multi-modal deformable registration. *Medical image analysis* 16, 1423–1435.
- Hermosillo, G., Chefd’Hotel, C., Faugeras, O., 2002. Variational methods for multimodal image matching. *International Journal of Computer Vision* 50, 329–343.
- Hill, D.L., Batchelor, P.G., Holden, M., Hawkes, D.J., 2001. Medical image registration. *Physics in medicine & biology* 46, R1.
- Hoffmann, M., Billot, B., Greve, D.N., Iglesias, J.E., Fischl, B., Dalca, A.V., 2021. Synthmorph: learning contrast-invariant registration without acquired images. *IEEE Transactions on Medical Imaging* 41, 543–558.

- Hoffmann, M., Billot, B., Greve, D.N., Iglesias, J.E., Fischl, B., Dalca, A.V., 2022. SynthMorph: Learning contrast-invariant registration without acquired images. *IEEE Transactions on Medical Imaging* 41, 543–558. URL: <https://doi.org/10.1109/tmi.2021.3116879>, doi:10.1109/tmi.2021.3116879.
- Hoopes, A., Hoffmann, M., Fischl, B., Gutttag, J., Dalca, A.V., 2021. Hypermorph: Amortized hyperparameter learning for image registration. *IPMI*.
- Hu, Y., Modat, M., Gibson, E., Ghavami, N., Bonmati, E., Moore, C.M., Emberton, M., Noble, J.A., Barratt, D.C., Vercauteren, T., 2018a. Label-driven weakly-supervised learning for multimodal deformable image registration, in: 2018 IEEE 15th International Symposium on Biomedical Imaging (ISBI 2018), IEEE. pp. 1070–1074.
- Hu, Y., Modat, M., Gibson, E., Li, W., Ghavami, N., Bonmati, E., Wang, G., Bandula, S., Moore, C.M., Emberton, M., et al., 2018b. Weakly-supervised convolutional neural networks for multimodal image registration. *Medical image analysis* 49, 1–13.
- Jaderberg, M., Simonyan, K., Zisserman, A., Kavukcuoglu, K., 2015. Spatial transformer networks. *arXiv preprint arXiv:1506.02025*.
- Kingma, D.P., Ba, J., 2017. Adam: A method for stochastic optimization. *arXiv preprint arXiv:1412.6980* *arXiv:1412.6980*.
- Kleesiek, J., Urban, G., Hubert, A., Schwarz, D., Maier-Hein, K., Bendszus, M., Biller, A., 2016. Deep mri brain extraction: A 3d convolutional neural network for skull stripping. *NeuroImage* 129, 460–469.
- Krebs, J., Delingette, H., Mailhé, B., Ayache, N., Mansi, T., 2019. Learning a probabilistic model for diffeomorphic registration. *IEEE transactions on medical imaging* 38, 2165–2176.
- Lee, M.C., Oktay, O., Schuh, A., Schaap, M., Glocker, B., 2019a. Image-and-spatial transformer networks for structure-guided image registration, in: International Conference on Medical Image Computing and Computer-Assisted Intervention, Springer. pp. 337–345.
- Lee, M.C.H., Oktay, O., Schuh, A., Schaap, M., Glocker, B., 2019b. Image-and-spatial transformer networks for structure-guided image registration. *arXiv:1907.09200*.
- Lenc, K., Vedaldi, A., 2016. Learning covariant feature detectors, in: European conference on computer vision, Springer. pp. 100–117.
- Liu, F., Yan, K., Harrison, A., Guo, D., Lu, L., Yuille, A., Huang, L., Xie, G., Xiao, J., Ye, X., Jin, D., 2021. Same: Deformable image registration based on self-supervised anatomical embeddings. *arXiv:2109.11572*.
- Lowe, D.G., 2004. Distinctive image features from scale-invariant keypoints. *International journal of computer vision* 60, 91–110.
- Ma, J., Jiang, X., Fan, A., Jiang, J., Yan, J., 2021. Image matching from handcrafted to deep features: A survey. *International Journal of Computer Vision* 129, 23–79.
- Ma, T., Gupta, A., Sabuncu, M.R., 2020. Volumetric landmark detection with a multi-scale shift equivariant neural network. *International Symposium on Biomedical Imaging (ISBI)*, 981–985.
- Matas, J., Chum, O., Urban, M., Pajdla, T., 2004. Robust wide-baseline stereo from maximally stable extremal regions. *Image and vision computing* 22, 761–767.
- Mattes, D., Haynor, D.R., Vesselle, H., Lewellen, T.K., Eubank, W., 2003. Pet-ct image registration in the chest using free-form deformations. *IEEE transactions on medical imaging* 22, 120–128.
- Mocanu, S., Moody, A.R., Khademi, A., 2021. Flowreg: Fast deformable unsupervised medical image registration using optical flow. *arXiv preprint arXiv:2101.09639*.
- Mok, T.C.W., Chung, A.C.S., 2021. Conditional deformable image registration with convolutional neural network.
- Montesinos, P., Gouet, V., Deriche, R., 1998. Differential invariants for color images, in: Proceedings. Fourteenth International Conference on Pattern Recognition (Cat. No. 98EX170), IEEE. pp. 838–840.

- Oliveira, F.P., Tavares, J.M.R., 2014. Medical image registration: a review. *Computer methods in biomechanics and biomedical engineering* 17, 73–93.
- Ono, Y., Trulls, E., Fua, P., Yi, K.M., 2018. Lf-net: Learning local features from images. *arXiv preprint arXiv:1805.09662*.
- Qin, C., Shi, B., Liao, R., Mansi, T., Rueckert, D., Kamen, A., 2019. Unsupervised deformable registration for multi-modal images via disentangled representations. *Lecture Notes in Computer Science Information Processing in Medical Imaging*, 249–261doi:10.1007/978-3-030-20351-1_19.
- Rohr, K., Stiehl, H., Sprengel, R., Buzug, T., Weese, J., Kuhn, M., 2001. Landmark-based elastic registration using approximating thin-plate splines. *IEEE Transactions on Medical Imaging* 20, 526–534. doi:10.1109/42.929618.
- Rosenfeld, A., Thurston, M., 1971. Edge and curve detection for visual scene analysis. *IEEE Transactions on computers* 100, 562–569.
- Sofka, M., Milletari, F., Jia, J., Rothberg, A., 2017. Fully convolutional regression network for accurate detection of measurement points, in: *Deep learning in medical image analysis and multimodal learning for clinical decision support*. Springer, pp. 258–266.
- Song, X., Chao, H., Xu, X., Guo, H., Xu, S., Turkbey, B., Wood, B.J., Sanford, T., Wang, G., Yan, P., 2022. Cross-modal attention for multi-modal image registration. *Medical Image Analysis* 82, 102612. URL: <https://www.sciencedirect.com/science/article/pii/S1361841522002407>, doi:https://doi.org/10.1016/j.media.2022.102612.
- Sotiras, A., Davatzikos, C., Paragios, N., 2013. Deformable medical image registration: A survey. *IEEE Transactions on Medical Imaging* 32, 1153–1190. doi:10.1109/TMI.2013.2265603.
- Toews, M., Zöllei, L., Wells, W.M., 2013. Feature-based alignment of volumetric multi-modal images, in: *International Conference on Information Processing in Medical Imaging*, Springer. pp. 25–36.
- Tuytelaars, T., Mikolajczyk, K., 2008. Local invariant feature detectors: a survey. Now Publishers Inc.
- Uluđag, K., Roebroek, A., 2014. General overview on the merits of multimodal neuroimaging data fusion. *Neuroimage* 102, 3–10.
- Ulyanov, D., Vedaldi, A., Lempitsky, V., 2016. Instance normalization: The missing ingredient for fast stylization. *arXiv preprint arXiv:1607.08022*.
- Uzunova, H., Wilms, M., Handels, H., Ehrhardt, J., 2017. Training cnns for image registration from few samples with model-based data augmentation, in: *International Conference on Medical Image Computing and Computer-Assisted Intervention*, Springer. pp. 223–231.
- Verdie, Y., Yi, K., Fua, P., Lepetit, V., 2015. Tilde: A temporally invariant learned detector, in: *Proceedings of the IEEE Conference on Computer Vision and Pattern Recognition*, pp. 5279–5288.
- Viola, P., Wells III, W.M., 1997. Alignment by maximization of mutual information. *International journal of computer vision* 24, 137–154.
- de Vos, B.D., Berendsen, F.F., Viergever, M.A., Sokooti, H., Staring, M., Išgum, I., 2019. A deep learning framework for unsupervised affine and deformable image registration. *Medical image analysis* 52, 128–143.
- de Vos, B.D., Berendsen, F.F., Viergever, M.A., Staring, M., Išgum, I., 2017. End-to-end unsupervised deformable image registration with a convolutional neural network, in: *Deep learning in medical image analysis and multimodal learning for clinical decision support*. Springer, pp. 204–212.
- Wachinger, C., Toews, M., Langs, G., Wells, W., Golland, P., 2018. Keypoint transfer for fast whole-body segmentation. *IEEE transactions on medical imaging* 39, 273–282.
- Wang, A.Q., Dalca, A.V., Sabuncu, M.R., 2022. Computing multiple image reconstructions with a single hypernetwork. *Machine Learning for Biomedical Imaging* 1.

- Van de Weijer, J., Gevers, T., Bagdanov, A.D., 2005. Boosting color saliency in image feature detection. *IEEE transactions on pattern analysis and machine intelligence* 28, 150–156.
- Wu, G., Kim, M., Wang, Q., Munsell, B.C., Shen, D., 2015. Scalable high-performance image registration framework by unsupervised deep feature representations learning. *IEEE Transactions on Biomedical Engineering* 63, 1505–1516.
- Yang, X., Kwitt, R., Styner, M., Niethammer, M., 2017. Quicksilver: Fast predictive image registration—a deep learning approach. *NeuroImage* 158, 378–396.
- Yi, K.M., Trulls, E., Lepetit, V., Fua, P., 2016. Lift: Learned invariant feature transform, in: *European conference on computer vision*, Springer. pp. 467–483.
- Yi, K.M., Trulls, E., Ono, Y., Lepetit, V., Salzmann, M., Fua, P., 2018. Learning to find good correspondences. *arXiv:1711.05971*.
- Yu, E.M., Wang, A.Q., Dalca, A.V., Sabuncu, M.R., 2022. Keymorph: Robust multi-modal affine registration via unsupervised keypoint detection, in: *Medical Imaging with Deep Learning*.
- Zhang, J., Wang, Y., Dai, J., Cavichini, M., Bartsch, D.U.G., Freeman, W.R., Nguyen, T.Q., An, C., 2022. Two-step registration on multi-modal retinal images via deep neural networks. *IEEE Transactions on Image Processing* 31, 823–838. doi:10.1109/TIP.2021.3135708.
- Zhang, R., 2019. Making convolutional networks shift-invariant again. *arXiv:1904.11486*.

Appendix A. Derivation of Eq. (3)

We wish to find the optimal affine transformation $A \in \mathbb{R}^{D \times (D+1)}$ which minimizes:

$$\begin{aligned}\mathcal{L} &= \sum_{i=1}^N \left(A\tilde{\mathbf{p}}^{(i)} - \mathbf{q}^{(i)} \right)^2 \\ &= \|A\tilde{\mathbf{P}} - \mathbf{Q}\|_F^2,\end{aligned}$$

where $\|\cdot\|_F$ denotes the Frobenius norm. Taking the derivative with respect to A and setting the result to zero, we obtain:

$$\begin{aligned}\frac{\partial \mathcal{L}}{\partial A} &= (A\tilde{\mathbf{P}} - \mathbf{Q})\tilde{\mathbf{P}}^T = \mathbf{0} \\ \Rightarrow A\tilde{\mathbf{P}}\tilde{\mathbf{P}}^T &= \mathbf{Q}\tilde{\mathbf{P}}^T \\ \Rightarrow A &= \mathbf{Q}\tilde{\mathbf{P}}^T(\tilde{\mathbf{P}}\tilde{\mathbf{P}}^T)^{-1}.\end{aligned}$$

Appendix B. Additional Figures

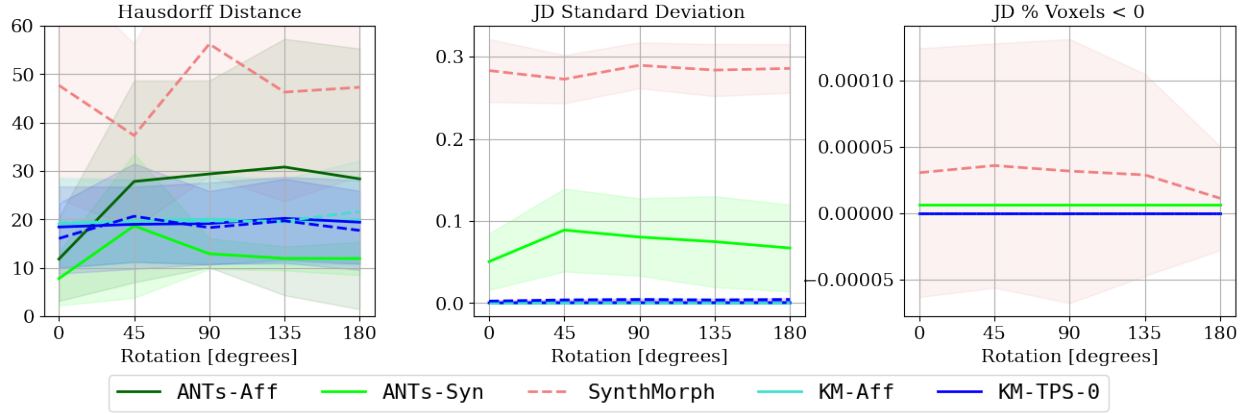


Figure B.16: KeyMorph and baseline model performance across rotation angle for various metrics. JD is short for Jacobian determinant. In the last panel, KeyMorph variants are 0 across all rotation angles. Hausdorff Distance is computed with respect to the brain surface only. Shaded regions denote standard deviation.

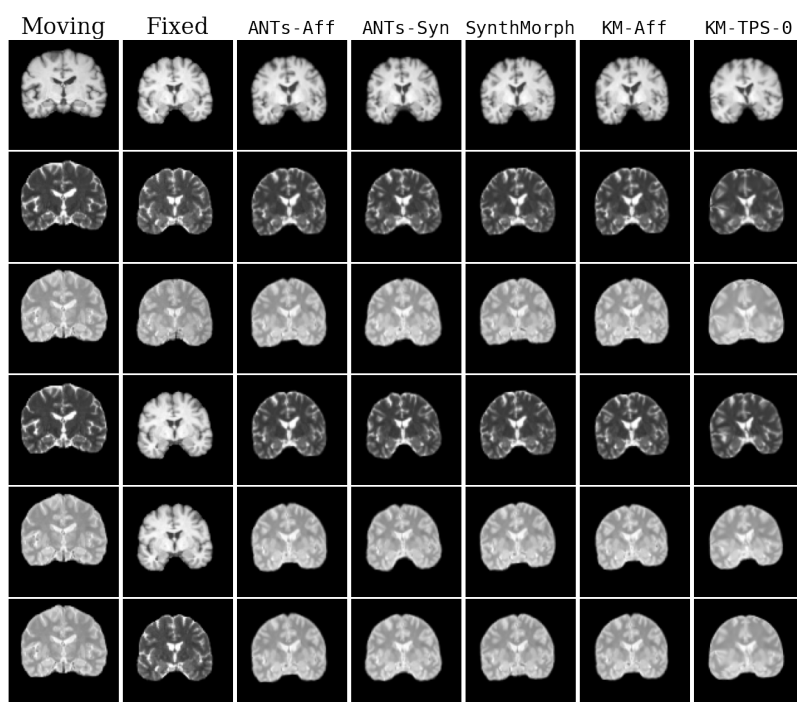


Figure B.17: Qualitative results for all models. Moving image is not misaligned. DLIR results are omitted to save space.

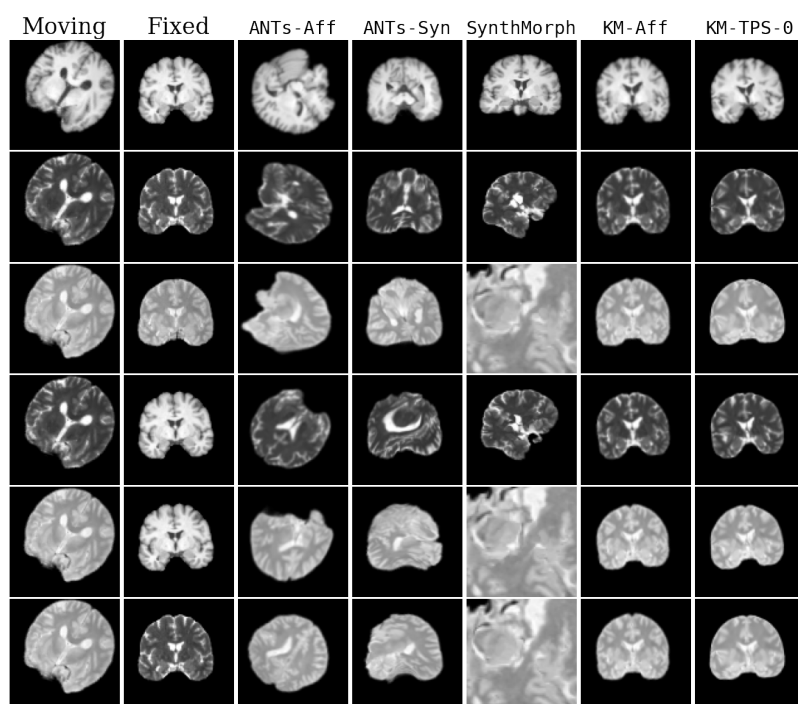


Figure B.18: Qualitative results for all models. Moving image is misaligned by 45° in each dimension. DLIR results are omitted to save space.

T	Model	Dice Score								
		T1→T1	T2→T1	PD→T1	T1→T2	T2→T2	PD→T2	T1→PD	T2→PD	PD→PD
rotation	No registration	20.28±19.80	12.67±12.52	18.68±15.56	12.67±12.52	24.02±22.28	18.46±16.99	18.68±15.56	18.46±16.99	19.67±19.65
	DLIR-Uni-180-unsup	26.8±14.84	-	-	-	26.86±15.01	-	-	-	29.36±17.01
	DLIR-Uni-35-unsup	51.33±7.95	-	-	-	53.88±7.2	-	-	-	53.57±6.35
	DLIR-Uni-180-sup	38.64±14.65	-	-	-	28.59±12.62	-	-	-	35.24±13.98
	DLIR-Uni-35-sup	52.57±7.81	-	-	-	53.41±9.33	-	-	-	54.14±8.03
	DLIR-Multi-180-unsup	21.68±11.06	21.78±11.42	22.0±11.46	21.32±10.6	21.88±11.48	21.99±11.37	21.22±10.67	21.78±11.5	22.09±11.62
	DLIR-Multi-35-sup	49.84±8.48	48.98±8.16	49.37±8.41	49.27±8.33	49.42±8.21	49.41±8.36	49.52±8.31	49.15±8.11	50.28±8.62
	ANTs-Aff	48.07±26.14	44.32±25.34	42.27±25.0	43.48±25.23	45.06±25.59	42.69±25.04	40.56±25.01	43.51±24.89	44.66±25.84
	ANTs-Syn	49.33±24.39	46.02±22.82	43.82±23.18	45.13±22.07	46.82±26.35	43.23±23.63	42.69±25.60	45.83±22.90	46.03±23.29
	SynthMorph	67.20±22.42	47.79±18.55	52.18±21.98	48.48±18.68	46.64±17.39	44.15±18.53	51.98±22.43	45.62±18.69	45.42±20.91
	KM-Aff-unsup	64.35±11.18	57.68±10.78	60.08±9.51	57.85±10.26	61.18±15.77	58.68±12.01	59.05±8.42	59.04±11.45	61.19±12.97
	KM-Aff-sup	67.56±9.39	61.69±5.34	62.46±6.42	61.40±10.62	63.16±5.3	61.11±4.83	63.44±4.87	61.11±5.11	63.32±5.26
	KM-TPS-0-unsup	61.33±6.56	53.23±5.99	53.65±5.78	52.60±6.07	59.62±6.28	55.21±6.57	54.22±6.01	54.77±5.68	56.72±6.21
	KM-TPS-0-sup	70.54 ± 5.11	65.29 ± 5.04	66.24 ± 4.82	65.29 ± 4.96	65.45 ± 5.36	63.89 ± 4.83	66.24 ± 4.87	63.56 ± 5.11	66.24 ± 5.26
scaling	No registration	22.33±14.24	12.28±13.28	14.24±15.94	12.28±13.28	25.23±19.02	19.24±12.34	14.24±15.94	19.24±12.34	22.34±14.24
	DLIR-Uni-180-unsup	45.97±8.07	-	-	-	45.96±8.46	-	-	-	53.47±7.32
	DLIR-Uni-35-unsup	53.32±7.26	-	-	-	54.46±7.37	-	-	-	53.37±5.98
	DLIR-Uni-180-sup	44.23±9.13	-	-	-	39.09±7.48	-	-	-	42.91±7.74
	DLIR-Uni-35-sup	55.19±6.95	-	-	-	54.92±7.96	-	-	-	57.57±6.8
	DLIR-Multi-180-unsup	39.12±9.49	41.08±7.93	41.32±7.81	38.12±9.45	41.74±8.43	41.72±8.18	37.96±9.93	41.48±8.85	42.02±8.81
	DLIR-Multi-35-sup	53.43±6.35	52.68±6.33	52.86±6.54	52.57±6.56	52.84±6.98	52.49±6.71	52.69±6.37	52.38±6.76	53.32±6.74
	ANTs-Aff	66.29±6.19	63.42±5.75	62.51±5.93	62.7±5.81	63.84±6.33	62.42±5.74	61.49±5.94	62.28±5.7	64.29±6.48
	ANTs-Syn	66.60±5.69	63.91±6.10	62.83±6.48	63.0±5.30	63.98±5.78	62.70±4.61	61.26±6.27	63.06±5.37	64.62±5.84
	SynthMorph	68.18±7.37	64.80 ± 6.21	63.84±6.13	64.21±5.28	65.39±7.26	64.70±6.30	63.18±6.52	63.27±5.14	65.13±6.82
	KM-Aff-unsup	63.0±6.79	59.23±6.02	59.7±6.65	59.35±6.13	61.73±6.49	60.27±6.01	59.66±6.28	60.16±5.62	62.8±6.64
	KM-Aff-sup	66.51±5.24	63.25±4.86	63.35±4.6	63.33±4.98	64.16±5.35	62.7±4.55	63.37±5.0	62.77±4.81	64.85±5.42
	KM-TPS-0-unsup	62.53±7.30	57.51±6.83	57.38±6.13	56.87±7.39	58.79±6.98	58.18±6.94	56.87±6.10	57.27±7.32	60.92±5.97
	KM-TPS-0-sup	69.23 ± 6.31	63.83±4.90	65.72 ± 5.17	66.29 ± 5.42	66.75 ± 4.98	64.84 ± 5.07	65.28 ± 5.82	65.81 ± 4.96	66.12 ± 5.03
translation	No registration	14.38±16.24	12.64±15.90	15.30±15.22	12.64±15.90	19.23±20.30	17.36±12.41	15.30±15.22	17.36±12.41	11.34±19.10
	DLIR-Uni-180-unsup	45.88±8.12	-	-	-	45.57±8.25	-	-	-	53.14±7.73
	DLIR-Uni-35-unsup	52.8±7.84	-	-	-	54.43±7.56	-	-	-	53.32±6.33
	DLIR-Uni-180-sup	45.05±8.84	-	-	-	38.59±7.28	-	-	-	43.09±8.07
	DLIR-Uni-35-sup	55.26±6.97	-	-	-	54.77±7.97	-	-	-	57.65±6.69
	DLIR-Multi-180-unsup	37.52±9.69	38.78±8.52	39.25±8.35	36.32±9.57	39.1±9.18	39.3±8.79	36.18±10.03	38.92±9.5	39.7±9.38
	DLIR-Multi-35-sup	53.41±6.17	52.38±6.07	52.67±6.5	52.84±6.27	52.78±6.58	52.6±6.68	52.88±6.49	52.33±6.62	53.33±6.93
	ANTs-Aff	66.34±6.37	63.45±5.7	62.49±5.9	62.79±5.81	63.94±6.46	62.44±5.73	61.5±5.97	62.34±5.72	64.3±6.62
	ANTs-Syn	66.70±5.83	63.81±5.35	62.18±5.30	63.01±6.04	63.53±5.91	63.30±5.02	62.06±4.98	62.70±6.41	64.09±6.06
	SynthMorph	69.13±7.71	63.45±5.7	64.20±6.45	64.31±6.50	65.80±7.13	64.24±6.31	63.58±6.73	64.80±6.30	66.58±7.31
	KM-Aff-unsup	63.5±7.09	59.5±5.92	59.84±6.64	59.86±6.02	62.33±6.63	60.58±5.9	60.19±6.19	60.64±5.5	63.28±6.78
	KM-Aff-sup	66.99±5.41	63.55±4.82	63.75±4.64	63.94±4.71	64.79±5.62	63.34±4.55	63.83±4.74	63.16±4.86	65.42±5.66
	KM-TPS-0-unsup	62.05±6.34	57.40±5.11	58.79±6.14	58.74±7.31	61.30±7.23	59.94±5.20	59.22±5.67	59.51±6.90	61.13±6.18
	KM-TPS-0-sup	70.60 ± 4.99	66.23 ± 5.85	65.82 ± 5.06	66.25 ± 5.13	66.82 ± 5.16	66.32 ± 5.10	65.30 ± 5.83	66.48 ± 5.31	68.13 ± 4.98

Table B.3: Mean performance of all methods ± standard deviation. The average Dice score is computed across test subject pairs, brain regions, and modalities. The notation $A \rightarrow B$ refers to registering moving volumes of modality A to fixed volumes of modality B . Bold numbers highlight the highest Dice score of a task given a transformation shown in the first column T.